Clustering Dynamic PET Images on the Projection Domain

Mustafa E. Kamasak and Bulent Bayraktar

***Abstract*—Segmentation of dynamic PET images is an important preprocessing step for kinetic parameter estimation. A single time activity curve (TAC) is extracted for each segmented region. This TAC is then used to estimate the kinetic parameters of the segmented region. Current methods perform this task in two independent steps; first dynamic positron emission tomography (PET) images are reconstructed from the projection data using conventional tomographic reconstruction methods, then the TAC of the pixels are clustered into a predetermined number of clusters. In this paper, we propose to cluster the regions of dynamic PET images directly on the projection data and simultaneously estimate the TAC of each cluster. This method does not require an intermediate step of tomographic reconstruction for each time frame. Therefore, the dimensionality of the estimation problem is reduced. The proposed method is compared with image-domain clustering methods based on weighted least squares (WLS) and expectation maximization with Gaussian mixtures methods (GMM-EM). Iterative coordinate descent (ICD) is used to reconstruct the emission images required by these methods. Simulation results show that the proposed method can substantially decrease the number of mislabeled pixels and reduce the root mean squared error (RMSE) of the cluster TACs.**

***Index Terms*—Clustering, dynamic PET, kinetic models, projection domain, regularization.**

I. Introduction

POSITRON emission tomography (PET) images generally have low signal-to-noise ratio (SNR) and the time activity curve (TAC) extracted from a single pixel may be very noisy. To improve the SNR, the TACs obtained from the physiologically similar pixels are averaged, and a single TAC is obtained for each group of pixels. Therefore, clustering physiologically similar pixels is an important preprocessing step. However, this is not a trivial task because of the low SNR and the partial volume effect of the PET images. In many PET studies clustering is performed manually by an operator. Manual clustering is an operator dependent and time consuming process. For improved reproducibility and faster clustering various automatic clustering algorithms are developed.

Ashburner *et al.* [1] proposed a modified mixture model algorithm. This algorithm computes the likelihood of each pixel TAC being in a cluster and iteratively maximizes this likelihood. Wong *et al.* [2] proposed a distance based clustering algorithm. Weighted distance between the pixel TACs within each cluster is minimized. This algorithm is further described in Section III.A. Chen *et al.* [3] used an expectation maximization (EM) based clustering algorithm with Markov random field (MRF) models. Brankov *et al.* [4] proposed a new distance metric between the pixel TACs and iteratively minimizes this distance within the pixel TACs of each cluster. Guo *et al.* [5], [6] proposed a hierarchical linkage based algorithm for clustering pixels. Automatic clustering can also be integrated into kinetic parameter estimation algorithms [7]. In some studies, segmentation is used to estimate the plasma input function from the PET images without arterial sampling [8], [9].

These clustering algorithms generally use pixel TACs as their feature vectors, which require reconstructed dynamic PET images. Sinogram data acquired with PET scanners are reconstructed using conventional tomographic reconstruction algorithms and TACs are extracted from these reconstructed images. In this paper, we propose a new algorithm which clusters the pixels on the projection domain. Therefore, it does not require tomographic reconstruction of dynamic PET images. A maximum *a priori* (MAP) based estimation framework is used for clustering pixels and computation of the cluster TACs. A similar algorithm was used by Frese *et al.* for discrete tomographic reconstruction of PET images [10]. We extended this algorithm for the unsupervised clustering of dynamic PET pixels directly on the projection domain.

This paper is organized as follows; Section II introduces the proposed method that clusters dynamic PET images directly on the projection domain. Section III briefly describes the conventional image-domain clustering algorithms. The simulation results are given in Section IV.

II. Unsupervised Clustering on Projection Domain

This section describes the unsupervised clustering algorithm on the projection domain. We introduce some notation, give some brief information on the scanner model, and then describe our MAP framework.

Assume that the data is collected at K time frames, and there are L clusters in the image. Each cluster has an associated TAC and a set of pixels that belongs to this cluster. For cluster l, let $\mu_l = [\mu_{l0}, \ldots, \mu_{l(K-1)}]$ denote the TAC of the cluster, and let $\mathcal{C}_l$ denote the set of pixels that belongs to this cluster. Let μ denote $L \times K$ matrix formed as $\mu = [\mu_0, \mu_1, \ldots, \mu_{L-1}]^T$ where superscript T denotes the matrix transpose. Let Ω denote the label image, ie. $\Omega = \{\Omega_0, \ldots, \Omega_{L-1}\}$. Given the sinogram measurements, denoted by Y, the MAP estimates of μ and Ω are

$$(\mu, \Omega) \leftarrow \arg\max p(\mu, \Omega | Y), \tag{1}$$

where $p(\cdot)$ denotes the probability.

Manuscript received March 8, 2006; revised December 10, 2006.

M. E. Kamasak is with Istanbul Technical University, Istanbul 34390, Turkey (e-mail: kamasak@itu.edu.tr).

B. Bayraktar is with Purdue University, West Lafayette, IN 47907 USA (e-mail: bayrakta@ecn.purdue.edu).

Color versions of one or more of the figures in this paper are available online at http://ieeexplore.ieee.org.

Digital Object Identifier 10.1109/TNS.2007.893325

In the following sections we formulate $p(\mu,\Omega|Y)$ and then we describe how to estimate (μ,Ω) iteratively and efficiently.

A. Scanner Model

Let Y_{mk} denote the sinogram measurement for projection $0 \leq m < M$ and time frame $0 \leq k < K$, and let Y be the $M \times K$ matrix of independently distributed Poisson random variables that form the sinogram measurements. Furthermore, let A be the forward projection matrix, with elements A_{ms}. A_{ms} denotes the probability of an emission from pixel s being detected by the mth detector pair. Then, the expected number of counts for each measurement at a given time, t_k is given by

$$E[Y_{mk}|\mu,\Omega] = \sum_{l=0}^{L-1} \sum_{s\in\Omega_l} A_{ms}\mu_{lk}. \tag{2}$$

For simplicity of notation let's define

$$Q_{ml}(\Omega) = \sum_{s\in\Omega_l} A_{ms}, \tag{3}$$

$$Q_m(\Omega) = [Q_{m0},\ldots,Q_{m(L-1)}], \tag{4}$$

and

$$Q(\Omega) = \begin{bmatrix} Q_0 \\ \vdots \\ Q_{M-1} \end{bmatrix}. \tag{5}$$

Then (2) can be compactly expressed in the matrix notation as

$$E[Y|\mu,\Omega] = Q(\Omega)\mu. \tag{6}$$

Using this notation we can show that the probability density function for the measured sinogram is [11]

$$p(Y|\mu,\Omega) = \prod_{k=0}^{K-1}\prod_{m=0}^{M-1} \frac{(Q_m(\Omega)\mu_{*k})^{Y_{mk}} e^{-(Q_m(\Omega)\mu_{*k})}}{Y_{mk}!} \tag{7}$$

where μ_{*k} is the kth column of μ. The log likelihood of the sinogram matrix is then given by

$$\mathrm{LL}(Y|\mu,\Omega) = \sum_{k=0}^{K-1}\sum_{m=0}^{M-1} Y_{mk}\log(Q_m(\Omega)\mu_{*k}) - (Q_m(\Omega)\mu_{*k}) - \log(Y_{mk}!). \tag{8}$$

B. Estimation Framework

A cost function can be formed by negating the log likelihood given in (8) and adding a regularization function, $S(\Omega)$.

$$C(Y|\mu,\Omega) = -\mathrm{LL}(Y|\mu,\Omega) + S(\Omega). \tag{9}$$

The regularization function penalizes the local label changes and therefore it controls the spatial continuity of pixel labels. This type of regularizaton function was used by Besag [12] for image clustering.

The regularization function can be obtained from an assumed prior distribution of the label image. In this work, we model the label image as a Markov random field (MRF) with Gibbs distribution. The likelihood of a particular label image, Ω is then

$$p(\Omega) = \frac{1}{Z}\exp\left\{-\beta \sum_{s,r\in\mathcal{N}} g_{s-r}(1-\delta(\omega_s,\omega_r))\right\}, \tag{10}$$

where Z is the normalization constant, $\mathcal{N}$ is the set of all spatially neighboring pixel pairs in Ω, g_{s-r} is the coefficient linking pixels s and r, β is a constant that controls the spatial smoothness of the label image, and $\delta(\cdot,\cdot)$ denotes the Kronecker delta function.

In this paper, $\mathcal{N}$ is formed by 8-point spatial neighborhood. We choose the negative logarithm of (10) as our regularization function, i.e.,

$$S(\Omega) = \beta \sum_{s,r\in\mathcal{N}} g_{s-r}(1-\delta(\omega_s,\omega_r)). \tag{11}$$

Note that with this regularization function, high values of the regularization parameter, β, will correspond to spatially smoother label images. We can similarly add another regularization function for the temporal smoothness of the cluster TACs.

C. Clustering With Iterative Coordinate Descent Clustering (CICD)

There is no closed form expression for the minimization of the cost function given in (9). Therefore, we used an iterative minimization technique that we named clustering with iterative coordinate descent (CICD). It is a modified version of iterative coordinate descent (ICD) algorithm used in conventional PET image reconstruction [11].

A CICD iteration has two steps; first the cluster TACs are fixed and pixel labels are sequentially updated to minimize the cost function. When all pixel labels are updated, the cluster TACs are updated to minimize the cost function. Therefore, with each CICD iteration, the cost function given in (9) monotonically decreases.

1) Pixel Label Update: Assume that we know all cluster TACs and we fix them during the update of pixel labels. Let ω_s denote the current label of pixel s, and we want to change it to be $\tilde{\omega}_s$ in this iteration so that the change in the cost function is minimized. If we change the label of pixel s from ω_s to $\tilde{\omega}_s$, the change in the cost function is

$$\Delta C(Y|\omega_s,\tilde{\omega}_s) = C(Y|\omega_s) - C(Y|\tilde{\omega}_s). \tag{12}$$

The evaluation of cost function requires re-computation of log likelihood, which leads to prohibitive computational complexity. Instead of computing the whole log likelihood, we compute the change in the log likelihood.

$$\begin{aligned}\Delta\mathrm{LL}(Y|\omega_s,\tilde{\omega}_s) &= \mathrm{LL}(Y|\tilde{\omega}_s) - \mathrm{LL}(Y|\omega_s) \\ &= \sum_{k=0}^{K-1}\sum_{m=0}^{M-1}\left\{A_{ms}(\mu_{\tilde{\omega}_s k} - \mu_{\omega_s k}) - Y_{mk}\log\left(A_{ms}(\mu_{\tilde{\omega}_s k} - \mu_{\omega_s k}) + \sum_{l=0}^{L-1} Q_{ml}\mu_{lk}\right)\right\}.\end{aligned} \tag{13}$$

Using the changes in the regularization function that only depend on the current pixel, the change in the cost function can be written as

$$\Delta C(Y|\omega_s,\tilde{\omega}_s) = \Delta\mathrm{LL}(Y|\omega_s,\tilde{\omega}_s) + \beta\sum_{r\in\partial s} g_{s-r}(1-\delta(\tilde{\omega}_s,\omega_r)), \tag{14}$$

where ∂s denotes the set of pixels that are neighbors of pixel s. Then the label of each pixel is updated as

$$\tilde{\omega}_s \leftarrow \arg\min \Delta C(Y|\omega_s, \tilde{\omega}_s). \tag{15}$$

This minimization is performed by simply searching through all possible (L) values of $\tilde{w}_s$. For efficient implementation, $\{Q_{ml}\}_{l=0}^{L-1}$ can be stored in the memory. Whenever a pixel label is updated $\{Q_{ml}\}_{l=0}^{L-1}$ can also be updated as follows

$$\begin{aligned} Q_{m\omega_s} &\leftarrow Q_{m\omega_s} - A_{ms} \\ Q_{m\tilde{\omega}_s} &\leftarrow Q_{m\tilde{\omega}_s} + A_{ms} \quad \text{for } m = 0 \cdots M-1. \end{aligned} \tag{16}$$

2) Cluster Tac Update: Once all the pixel labels are updated, we can update the cluster TACs. The cluster TACs are also updated as follows to minimize the cost function given in (9):

$$\tilde{\mu}_l \leftarrow \Delta C(Y|\mu_l, \tilde{\mu}_l) \tag{17}$$

where

$$\begin{aligned} \Delta C(Y|\mu_l, \tilde{\mu}_l) &= C(Y|\mu_l) - C(Y|\tilde{\mu}_l) \\ &= \mathrm{LL}(Y|\tilde{\mu}_l) - \mathrm{LL}(Y|\mu_l) \\ &= \Delta\mathrm{LL}(Y|\mu_l, \tilde{\mu}_l) \end{aligned} \tag{18}$$

$$\begin{aligned} \Delta\mathrm{LL}(Y|\mu_l, \tilde{\mu}_l) = \sum_{k=0}^{K-1}\sum_{m=0}^{M-1} Y_{mk}(&\log(Q_m(\Omega)\tilde{\mu}_l) \\ &-\log(Q_m(\Omega)\tilde{\mu}_l) - Q_m(\Omega)(\tilde{\mu}_l - \mu_l). \end{aligned} \tag{19}$$

The value of $\Delta\mathrm{LL}(Y|\mu_l, \tilde{\mu}_l)$ can be locally approximated with a second-order Taylor series as

$$\Delta\mathrm{LL}(Y|\mu_l, \tilde{\mu}_l) = \theta_1^T(\tilde{\mu}_l - \mu_l) + \frac{1}{2}(\tilde{\mu}_l - \mu_l)^T\theta_2(\tilde{\mu}_l - \mu_l) \tag{20}$$

where $\theta_1 = [\theta_{10}, \ldots, \theta_{1(K-1)}]^T$ and $\theta_2 = \mathrm{diag}\{\theta_{2kk}\}$ are the first and the second derivative of the log likelihood function with respect to μ_l. The first and second derivatives at time frame k are

$$\theta_{1k} \leftarrow \sum_{m=0}^{M-1}\left\{Q_{ml}\left(1 - \frac{Y_{mk}}{\sum_{l=0}^{L-1} Q_{ml}\mu_{lk}}\right)\right\} \tag{21}$$

$$\theta_{2kk} \leftarrow \sum_{m=0}^{M-1} Y_{mk}\left(\frac{Q_{ml}}{\sum_{l=0}^{L-1} Q_{ml}\mu_{lk}}\right)^2. \tag{22}$$

Using these derivative values given in (21), (22) cluster TACs can be computed simply as

$$\tilde{\mu}_l = \mu_l - \theta_2^{-1}\theta_1. \tag{23}$$

III. Image-Domain Clustering Algorithms

Image domain clustering algorithms use TACs extracted from emission images. The emission images are reconstructed using conventional PET reconstruction algorithms. Let x_{sk} be the reconstructed emission rate for pixel s at time frame k, and $x_s = [x_{s0}, \ldots, x_{s(K-1)}]$ be the reconstructed time response of pixel s.

A. Weighted Least Squares Clustering (WLS)

This algorithm minimizes the weighted square distance between the pixel TACs and the cluster TACs, ie.

$$(\mu, \Omega) \leftarrow \arg\min_{\mu,\Omega} \sum_{l=0}^{L-1}\sum_{s\in\Omega_l} ||x_s - \mu_l||_W^2, \tag{24}$$

where W is a weight matrix, and $||x||_W^2$ denotes x^TWx. In this work we used a diagonal weighting matrix formed as $W = \mathrm{diag}\{\Delta t_k\}_{k=0}^{K-1}$ where Δt_k is the duration of kth time frame.

This algorithm also iteratively updates the pixel labels and cluster TACs. Each iteration consists of two steps. In the first step, labels of pixels are sequentially updated. The label of a pixel is updated as follows:

$$\tilde{\omega}_s \leftarrow \arg\min_l ||x_s - \mu_l||_W^2. \tag{25}$$

After all pixel labels are updated, the cluster TACs are updated as follows to decrease the weighted distance given in (24).

$$\mu_l = \frac{1}{|\Omega_l|}\sum_{s\in\Omega_l} x_s, \tag{26}$$

where $|\Omega_l|$ denotes the number of pixels that are labeled as l. Each WLS iteration monotonically decreases the cost function, and iterations are repeated until the stopping (convergence) criteria is reached.

B. Gaussian Mixture Model With Expectation Maximization (GMM-EM)

It can be assumed that the pixel TACs are Gaussian distributed around the cluster TACs. Similar to other clustering methods pixel labels and cluster TACs can be updated iteratively.

Let R_l denote the covariance matrix of cluster l, and π_l denote the probability of cluster l. The posterior probability of a pixel being in cluster l, given its time response is

$$\begin{aligned} p(\omega_s = l|x_s, \mu_l) = &\frac{\pi_l}{(2\pi)^{K/2}}|R_l|^{-1/2} \\ &\times \exp\left\{-\frac{1}{2}(x_s - \mu_l)^T R_l^{-1}(x_s - \mu_l)\right\}. \end{aligned} \tag{27}$$

If the TACs and covariance matrices of the clusters are known, we can assign pixel labels to maximize the posterior, ie.

$$\begin{aligned} \omega_s \leftarrow \arg\min_l \Big\{&\frac{1}{2}(x_s - \mu_l)^T R_l^{-1}(x_s - \mu_l) \\ &+\frac{1}{2}\log|R_l| - \log(\pi_l)\Big\}. \end{aligned} \tag{28}$$

Once the labels are assigned the cluster TACs and covariance matrices can be updated using the EM algorithm [13].

C. Initialization of Clustering Algorithms

All clustering algorithms described above require initial cluster TACs, pixel labels, or both. It is possible to initialize

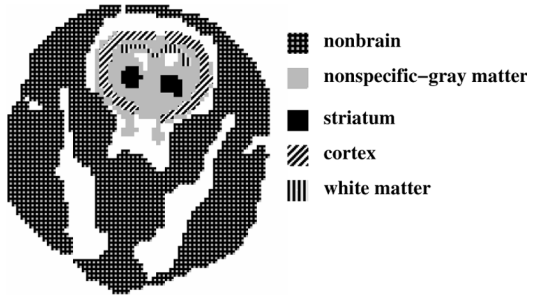

Fig. 1. Single-slice rat phantom. Regions of the rat phantom were derived from a segmented MR image. Different fill patterns indicate kinetically distinct tissue regions. Striatum is a region containing specific receptors for the tracer. Nonspecific-gray matter is tissue containing no specific binding sites for tracer but comparable blood flow parameters to striatal area; cortex is modeled as containing low concentration of binding sites; white matter in our dynamic phantom contains no specific binding sites and low flow;non-brain, which comprises much of the slice has fast influx and efflux of tracer. Solid white areas in figure represent a mixture of background regions that do not contain any activity over time. The small white areas dorsal to (above) the striatum are ventricles that contain cerebral spinal fluid and no tracer. White areas surrounding brain correspond to skull which does not take up appreciable amounts of tracer.

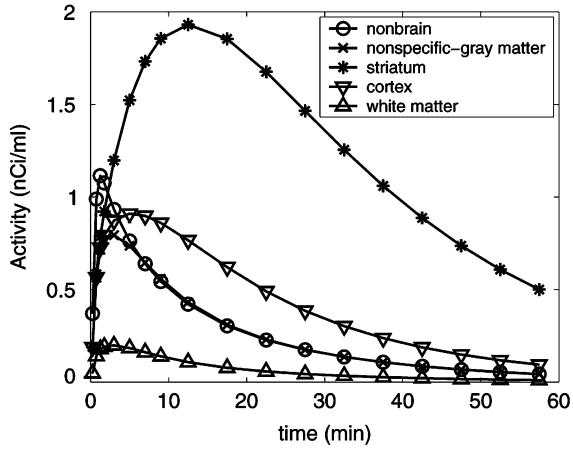

Fig. 2. Simulated time-activity curves for 5 distinct tissue regions in rat brain phantom.

these algorithms with randomly chosen initial labels and cluster TACs. However, arbitrary initial labels and cluster TACs may cause these algorithms to get stuck to local minima.

It is possible to initialize these algorithms with user selected clusters. A pixel from each cluster can be manually selected and their corresponding TACs can be used to initialize these algorithms. During this manual initialization, the number of clusters can be chosen by the user based on the prior anatomical knowledge or inspection of late-time frame reconstructions.

In the simulations described in Section IV.A, we initialized the algorithms by manually selected pixels and their TACs.

It is also possible to choose the number of clusters automatically by using information criteria such as Akaike Information Criteria (AIC) [14] or Schwarz Criteria (SC) [15], which can be incorporated to the cost function [2].

IV. Simulations

A. Phantom Design

Simulation experiments are based on a phantom of a rat's head. The phantom and kinetic parameters for the regions in this phantom are taken from Kamasak *et al.* [16]. Fig. 1 shows a schematic representation of the phantom and its regions. The phantom has six regions including the background. The regional TACs are shown in Fig. 2. For further details about the phantom see Kamasak *et al.* [16]. Time frames of emission images are generated using the phantom and the 2-tissue compartment model equations. The plasma function, $C_P(t)$, is generated using the second model in Wong *et al.* [17]. The blood contribution to the PET activity is assumed to be zero, and the tracer is assumed to be raclopride labeled with ^{11}C, which has a decay constant of $\lambda = 0.034$ min^{-1}. Total scan time is 60 min, divided into 18 time frames with 4×0.5 min, 4×2 min, and 10×5 min. The phantom resolution is 128×128 with each pixel having dimensions of (1.2 mm)^2. The data is not decay-corrected.

The rat phantom image at each time frame is forward projected into sinograms using a Poisson model for the detected counts. Each sinogram consists of 180 angles and 200 radial bins per angle. A triangular point spread function with a 4 mm base width is used in forward projections.

The image-domain clustering algorithms of Section III require that the emission images be reconstructed for each time frame. We used ICD image reconstruction with a quadratic prior and a regularization parameter for each time frame. The regularization parameters were chosen to minimize the total mean square error of the reconstructed emission image frames.

Both the CICD and image-domain clustering algorithms are stopped when none of the pixels change label during an iteration.

B. Performance Evaluation

Clustering algorithms are evaluated based on their performance of labeling pixels and estimating the cluster TACs. Two seperate performance measures are used: Misclassification percentage and RMSE of the cluster TACs.

Misclassification percentage, given in (29), is used to evaluate the labeling performance of the clustering algorithms. Misclassification percentage is computed as

$$\text{misclassification}(\%) = \frac{100}{N} \sum_{s=1}^{N} \left(1 - \delta\left(\omega_s^{\text{estimated}}, \omega_s^{\text{original}}\right)\right). \tag{29}$$

In (29), $\omega_s^{\text{estimated}}$ denotes the label of pixel s assigned by the proposed clustering algorithm, and $\omega_s^{\text{original}}$ denotes the correct label of pixel s.

The RMSE, given in (30), is used to evaluate the accuracy of the cluster TACs estimated by the clustering algorithms. The RMSE of the TAC estimations is computed as

$$\text{RMSE} = \sqrt{\frac{1}{K} \sum_{l=1}^{L} \left\| \mu_l^{\text{estimated}} - \mu_l^{\text{original}} \right\|^2}. \tag{30}$$

In (30), $\mu_l^{\text{estimated}}$ denotes the TAC for cluster l estimated by the proposed clustering algorithm, and μ_l^{original} is the correct TAC for cluster l.

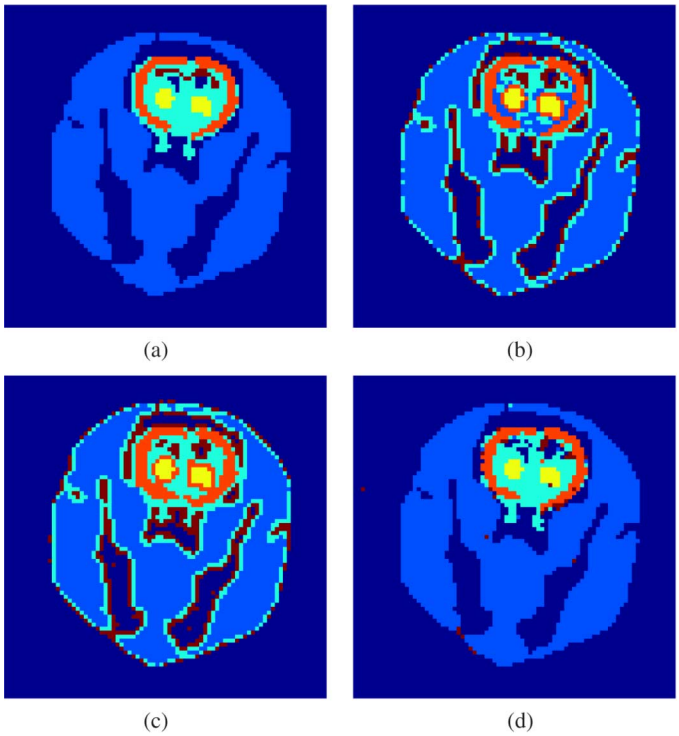

Fig. 3. Pixel labels assigned by the clustering algorithms. (a) Original. (b) ICD + WLS. (c) ICD + GMM − EM. (d) CICD.

TABLE I
PERCENTAGE OF MISLABELED PIXELS FOR THE CLUSTERING ALGORITHMS

method	misclassification (%)
ICD + WLS	5.41
ICD + GMM	6.23
CICD	0.44

V. SIMULATION RESULTS

The pixel labels assigned by the image-domain algorithms and the proposed method, CICD, are shown in Fig. 3. The images are clustered into six regions that are shown in Fig. 1. For these simulations, the regularization parameter, β, is set to five. This parameter is chosen empirically to minimize the misclassification percentage. The effects of the regularization parameter on clustering results are explained in Section V.A.

Visually it can be seen that CICD algorithm results have less mislabeled pixels than image-domain clustering methods. The percentage of mislabeled pixels for these algorithms are computed using (29) and given in Table I. From this table, it can be seen that the proposed clustering algorithm has the lowest mislabeled pixel percentage.

The cluster TACs estimated by the clustering algorithms are shown in Fig. 4. The root mean squared error for the cluster TACs are computed using (30) and listed in Table II. This table shows that for all regions except the white matter, the proposed algorithm have produced the lowest root mean squared error (RMSE) between the estimated cluster TACs and the actual cluster TACs.

Typical computation time for a CICD iteration is approximately 2.5 min. Image-domain algorithms take a few seconds (2–5 sec) per iteration. Computation times are given for a Pentium-V machine running Linux OS with 3 GHz processor and 1 GB memory. The convergence of the CICD algorithm (ie. until no change in the pixel labels) requires 20–25 iterations depending on the regularization parameter. With $\mathrm{beta} = 5$, the CICD algorithm converges after 22 iterations. For image-domain algorithms, convergence takes 30 iterations for ICD + WLS algorithm and 32 iterations for ICD + GMM − EM algorithm.

The success of the proposed CICD algorithm is due to the reduction in the number of estimated parameters. CICD algorithm assigns N labels and estimates $L \times K$ time points for cluster TACs. However, for image-domain clustering algorithms, the estimation of additional $N \times K$ emission rates for reconstructed emission images is required.

A. Effects of Regularization Parameter

The regularization parameter, β, adjusts the spatial smoothness of the label image. High regularization parameter increases the contribution of the image model to the cost function given in (9). Therefore, label images that deviate from the assumed image model are rejected with a high regularization parameter. On the other hand, low regularization parameter deemphasizes the image model and assigns the labels depending more on the acquired data. This allows the output label images to deviate from the image model. The regularization parameter should be chosen depending on the SNR of the data. As the SNR decreases, higher regularization parameter should be chosen to make the results less sensitive to the noise.

Using (11), we selected an image model that penalizes rapid label changes in a local pixel neighborhood. With this image model, CICD algorithm with high regularization parameter results in spatially smoother label images.

In Fig. 5, the results of the CICD algorithm with different regularization parameters are shown. From this figure, it can be seen that the label images obtained with low regularization parameters ($\beta = 1$ and $\beta = 3$) have rapid label changes which is not very likely in practice. As the regularization parameter increases, the label images become smoother. However, results with high regularization parameter ($\beta = 20$) have classification problems especially inside the brain region.

Fig. 6 shows the misclassification percentage in the results of the CICD algorithm with different regularization parameters. From this figure, we can conclude that the lowest misclassification percentage is obtained with $\beta = 5$.

Table III similarly shows the RMSE in the TAC results of the CICD algorithm with different regularization parameters. The TACs have high RMSE with low regularization parameters. Higher regularization parameters give comparable RMSE in the cluster TACs.

VI. CONCLUSION

We propose a new clustering algorithm that we call clustering with iterative coordinate descent (CICD). CICD clusters the dynamic PET images directly on the projection domain, and it does not require the intermediate step of emission reconstruction. The results of CICD algorithm are substantially better than the conventional image-domain clustering algorithms. It produces less

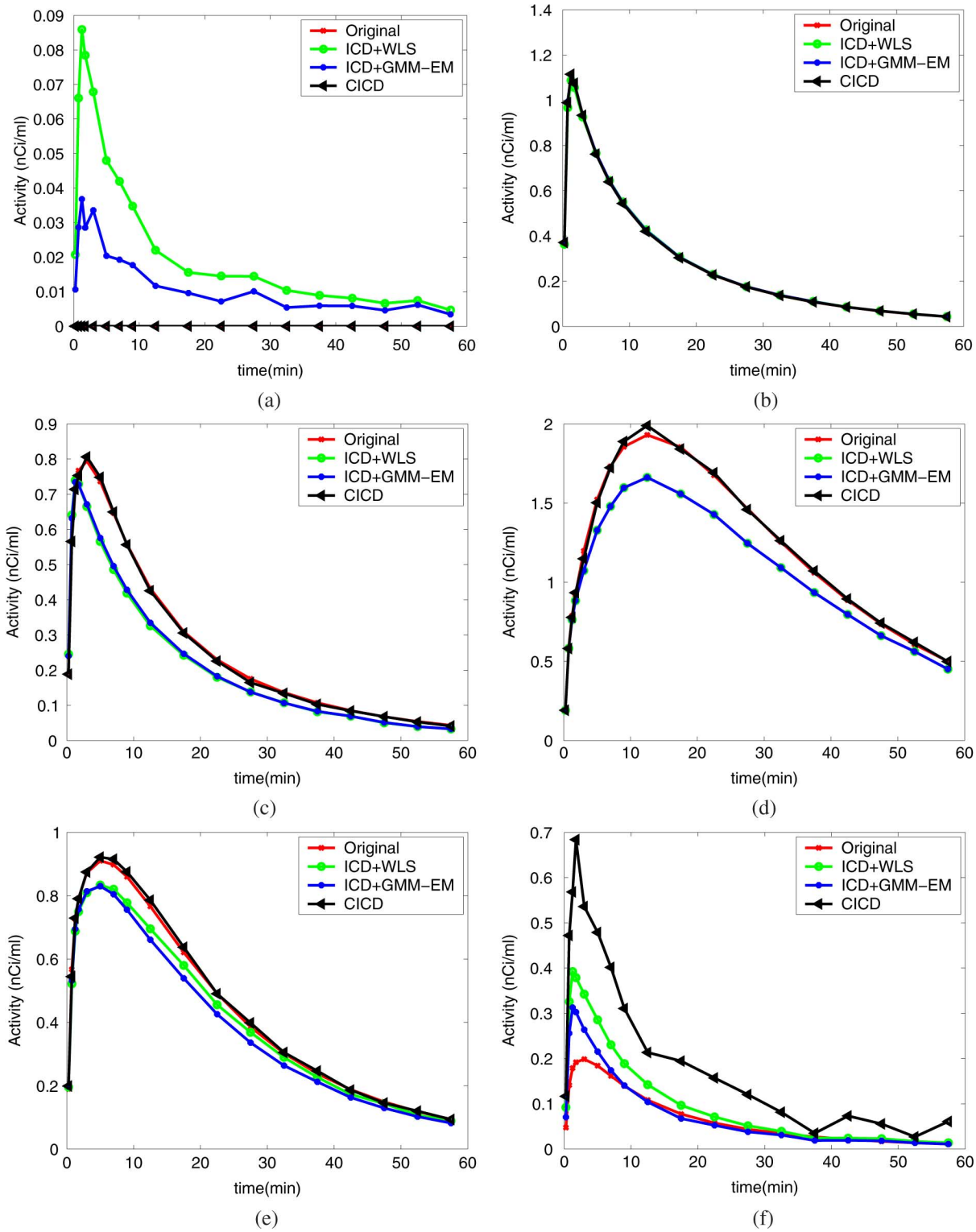

Fig. 4. Cluster TACs estimated by the clustering algorithms for each region in the rat head. (a) Background. (b) Nonbrain. (c) Nonspecific-gray matter. (d) Striatum. (e) Cortex. (f) White matter.

mislabeled pixels and estimates cluster TACs with lower RMSE than the image-domain clustering algorithms.

The proposed method has certain limitations. For example, in image-domain clustering methods it is possible to co-register the reconstructed images before the clustering. However, external measurement devices can allow us to record motion during the data acquisition and correct the data in an automated fashion [18].

More tests on real dynamic PET data are required for further analysis of this algorithm's merit. More flexible regularization strategies can also be integrated into this algorithm which may result in better clustering.

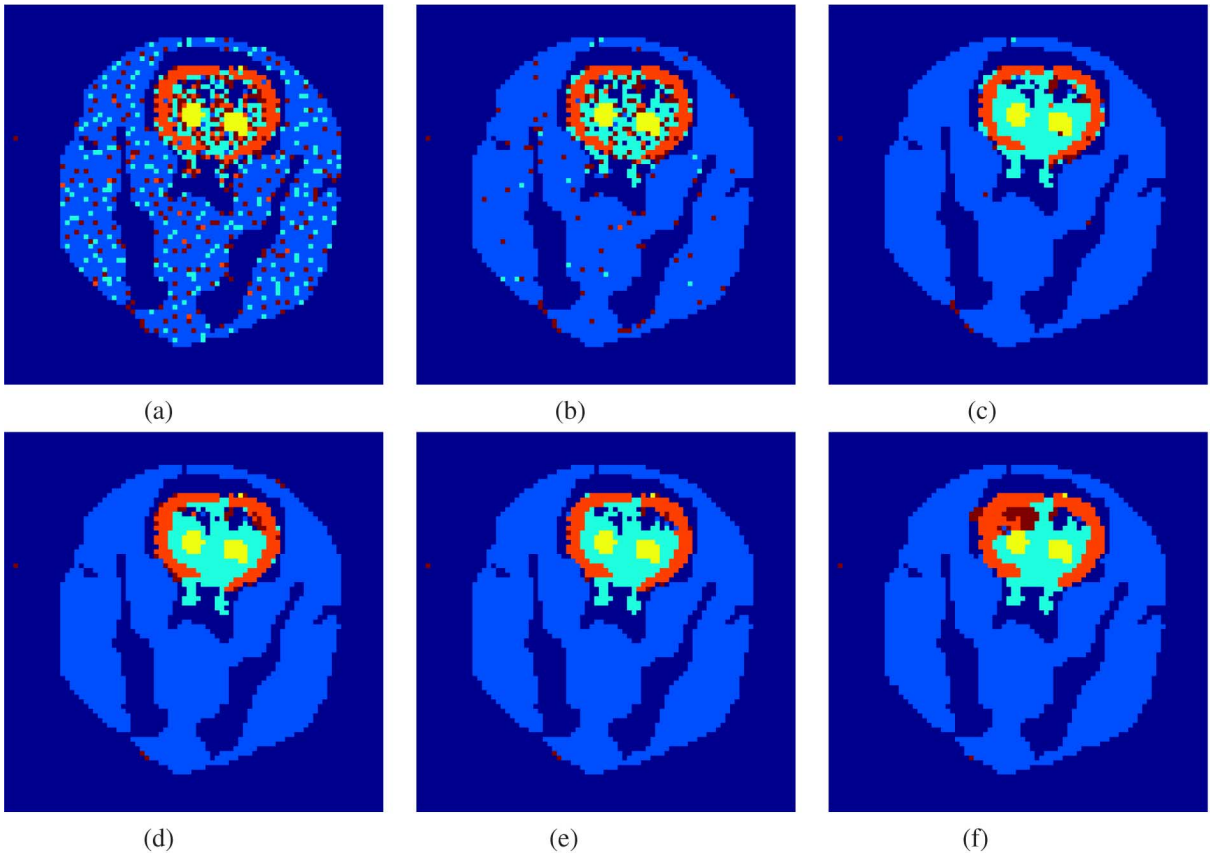

Fig. 5. Pixel labels assigned by the CICD algorithm with different regularization parameters. (a) $\beta = 1$. (b) $\beta = 3$. (c) $\beta = 5$. (d) $\beta = 8$. (e) $\beta = 12$. (f) $\beta = 20$.

TABLE II
RMSE OF THE CLUSTER TACS FOR EACH REGION IN THE RAT'S HEAD

region	WLS	GMM-EM	CICD
background	0.017	0.022	0.000
nonbrain	0.013	0.007	0.0004
nonspecific-gray matter	0.088	0.092	0.0063
striatum	0.207	0.239	0.0218
cortex	0.059	0.088	0.0110
white matter	0.059	0.019	0.2167

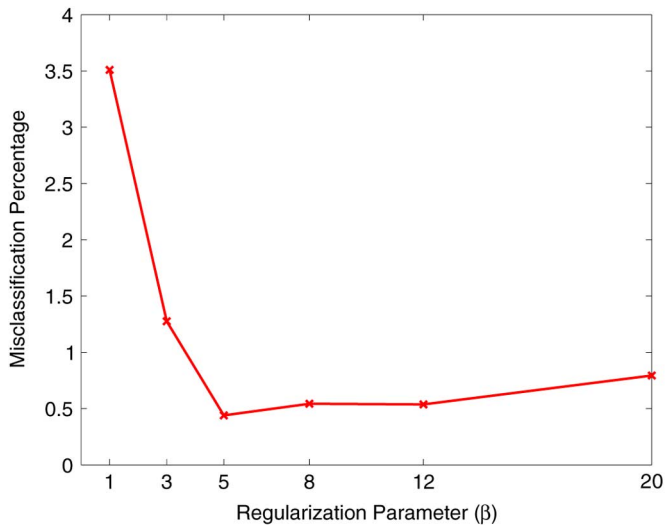

Fig. 6. Misclassification percentage of CICD algorithm with different regularization parameters.

TABLE III
RMSE OF THE CLUSTER TACS FOR EACH REGION IN THE RAT'S HEAD WITH DIFFERENT REGULARIZATION PARAMETERS

region	$\beta = 1$	$\beta = 3$	$\beta = 5$	$\beta = 8$	$\beta = 12$	$\beta = 20$
background	0	0	0	0	0	0
nonbrain	0.0345	0.0049	0.0004	0.0005	0.0004	0.0006
nonspecific-gray matter	0.0802	0.0748	0.0063	0.0052	0.0053	0.0081
striatum	0.0183	0.0231	0.0218	0.0204	0.0208	0.0185
cortex	0.0127	0.0111	0.0110	0.0149	0.0200	0.0395
white matter	0.2376	0.2445	0.2167	0.2171	0.2423	0.0830

REFERENCES

[1] J. Ashburner, J. Haslam, C. Taylor, V. J. Cunningham, and T. Jones, "A cluster analysis approach for the characterization of dynamic PET data," in *Quantification of Brain Function Using PET*, R. Myers, V. Cunningham, D. Bailey, and T. Jones, Eds. San Diego, CA: Academics, 1996, pp. 301–306.

[2] K.-P. Wong, D. Feng, S. R. Meikle, and M. J. Fulham, "Segmentation of dynamic PET images using cluster analysis," *IEEE Trans. Nucl. Sci.*, vol. 49, no. 1, pp. 200–207, Feb. 2002.

[3] J. L. Chen, S. R. Gunn, M. S. Nixon, and R. N. Gunn, "Markov random field models for segmentation of PET images," in *Proc. Information Processing in Medical Imaging*, 2001, vol. 2082, pp. 468–474.

[4] J. G. Brankov, N. P. Galatsanos, Y. Yang, and M. N. Wernick, "Segmentation of dynamic PET or fMRI images based on a similarity metric," *IEEE Trans. Nucl. Sci.*, vol. 50, no. 5, pp. 1410–1414, Oct. 2003.

[5] H. Guo, R. Renaut, and K. Chen, "Clustering for three dimensional kinetic PET data," in *Proc. IEEE Int. Conf. Data Mining, Clustering Large Data Sets, Workshop Notes*, Melbourne, FL, 2003, pp. 43–48.

[6] H. Guo, R. Renaut, K. Chen, and E. Reiman, "Clustering huge data sets for parametric PET imaging," *Biosystems*, vol. 71, no. 1–2, pp. 81–92, 2003.

[7] Y. Kimura, M. Senda, and N. Alpert, "Fast formation of statistically reliable FDG parametric images based on clustering and principal components," *Phys. Med. Biol.*, vol. 47, pp. 455–468, Aug. 2002.

[8] M. Liptrot, K. H. Adams, L. Martiny, L. H. Pinborg, M. N. Lonsdale, N. V. Olsen, S. Holm, C. Svarer, and G. M. Knudsen, "Cluster analysis in kinetic modelling of the brain: A noninvasive alternative to arterial sampling," *Neurolmage*, vol. 21, no. 2, pp. 483–493, 2004.

[9] K.-P. Wong, D. Feng, S. R. Meikle, and M. J. Fulham, "Non-invasive extraction of physiological parameters in quantitative PET studies using simultaneous estimation and cluster analysis," in *Proc. IEEE Medical Imaging Conf.*, Lyon, France, Oct. 2000, pp. 141–145.

[10] T. Frese, C. A. Bouman, and K. Sauer, , G. T. Herman and A. Kuba, Eds., "Multiscale bayesian methods for discrete tomography," in *Discrete Tomography: Foundations, Algorithms and Applications*. Cambridge, MA: Birkhauser, 1999, pp. 237–261.

[11] C. A. Bouman and K. Sauer, "A unified approach to statistical tomography using coordinate descent optimization," *IEEE Trans. Image Process.*, vol. 5, no. 3, pp. 480–492, Mar. 1996.

[12] J. Besag, "On the statistical analysis of dirty pictures," *J. Royal Statistical Society B*, vol. 48, no. 3, pp. 259–302, 1986.

[13] A. P. Dempster, N. M. Laird, and D. B. Rubin, "Maximum likelihood from incomplete data via the EM algorithm," *J. Royal Statistical Society B*, vol. 39, no. 1, pp. 1–38, 1977.

[14] H. Akaike, "A new look at the statistical model identification," *IEEE Trans. Autom. Control*, vol. AC-19, no. 6, pp. 716–723, Dec. 1974.

[15] G. Schwarz, "Estimating the dimension of a model," *Ann. Stat.*, vol. 6, pp. 461–464, 1978.

[16] M. E. Kamasak, C. A. Bouman, E. D. Morris, and K. Sauer, "Direct reconstruction of kinetic parameter images from dynamic PET data," *IEEE Trans. Med. Imag.*, vol. 24, no. 5, pp. 636–650, May 2005.

[17] K.-P. Wong, D. Feng, S. R. Meikle, and M. J. Fulham, "Simultaneous estimation of physiological parameters and the input function—In vivo PET data," *IEEE Trans. Inf. Technol. Biomed.*, vol. 5, no. 1, pp. 67–76, Mar. 2001.

[18] P. M. Bloomfield, T. J. Spinks, J. Reed, L. Schnorr, A. M. Westrip, L. Livieratos, R. Fulton, and T. Jones, "The design and implementation of a motion correction scheme for neurological PET," *Phys. Med. Biol.*, vol. 48, no. 8, pp. 959–978, 2003.